*Chinese Journal of*
**POLYMER SCIENCE**

RESEARCH ARTICLE

https://doi.org/10.1007/s10118-025-3425-4
*Chinese J. Polym. Sci.* **2025**, *43*, 2110–2117

# Metal-Organic Framework/Polyimide-Electrochemiluminescence Sensor for Enantioselective Detection of Histidine

Ye-Qian Ruan[a], Xuan Kuang[a*], and Rui Kuang[b*]

[a] *Key Laboratory of Interfacial Reaction & Sensing Analysis in Universities of Shandong, School of Chemistry and Chemical Engineering, University of Jinan, Jinan 250022, China*
[b] *College of Traffic Civil Engineering, Shandong Jiaotong University, Jinan 250023, China*

Electronic Supplementary Information

**Abstract** In this study, a novel linear polyimide chain (PTCDA-DCH) was used as an electrochemiluminescence (ECL) emitter, employing a chiral metal-organic framework (MOF) (Zn-Dcam-dabco) as the chiral selector and ferrocene (Fc) as a quencher to construct a chiral sensor for detecting histidine (His) enantiomers. Competitive interactions between Fc and His induce partial Fc desorption from the sensor surface, leading to ECL signal recovery. Differential Fc release due to the distinct binding affinities of Zn-Dcam-dabco for His enantiomers enabled precise chiral discrimination. Notably, the sensor achieved the quantitative detection of His enantiomers with an limits of detection (LOD) of 8 μmol/L. Furthermore, the sensor demonstrated excellent recovery rates of 98.0%–104% for l-histidine (L-His) and 92.0%–95.9% for D-His in spiked milk samples, validating its reliability for real-sample analysis. This study provides a promising platform for ECL-based chiral recognition, bioanalysis, and the rapid assessment of amino acids in food products.

**Keywords** Linear polyimide chain; MOF; Electrochemiluminescence; Enantioselective detection; Histidine

**Citation:** Ruan, Y. Q.; Kuang, X.; Kuang, R. Metal-organic framework/polyimide-electrochemiluminescence sensor for enantioselective detection of histidine. *Chinese J. Polym. Sci.* **2025**, *43*, 2110–2117.

## INTRODUCTION

Chirality, as a fundamental attribute of nature, plays a decisive role in the properties and functions of molecules in chemistry, biology and medicine.[1,2] In biological systems, enantiomeric differences in chiral molecules often lead to distinct bioactivity and physiological effects. For instance, l-histidine (L-His) is indispensable for protein biosynthesis and metabolic regulation.[3–5] However, conventional chiral analysis techniquessuch as high-performance liquid chromatography (HPLC),[6,7] capillary electrophoresis (CE),[8,9] and circular dichroism (CD)[10,11] spectroscopy have inherent limitations, including complex sample pretreatment, prolonged analysis time, and insufficient sensitivity, which hinder their applicability in modern bioanalysis and real-time on-site detection.

In this context, electrochemiluminescence (ECL) technology has emerged as a groundbreaking advancement in chiral analysis, owing to its unique signal amplification mechanism and ultrahigh sensitivity.[12,13] By leveraging efficient redox cycling to generate luminescent signals, ECL enables the trace-level detection of target molecules, offering a transformative approach for real-time chiral analysis in drug discovery and point-of-care diagnostics.[14,15] The emergence of polyimide (PI) provides an ideal platform for ECL detection. PI exhibits high stability, durability and efficient electron transport capability, which can significantly enhance charge carrier mobility and photoluminescence performance.[16–18]

Moreover, ferrocene (Fc) and its derivatives as novel ECL quenchers have demonstrated remarkable potential in biosensing owing to their reversible redox properties and efficient electron transfer capabilities.[19,20] Fc dynamically quenched ECL signals *via* electron transfer mechanisms, serving as a pivotal strategy for constructing sensitive signal switches. Complementing this, chiral metal-organic frameworks (CMOFs) have emerged as precise molecular recognition platforms owing to their superior chiral stability and host-guest interaction capabilities. For instance, the Zn-Dcam-dabco CMOF, constructed with D-camphoric acid (D-cam) as the chiral source, exhibited exceptional configurational stability and maintained robust chiral memory effects for high-precision enantiomeric discrimination.[21–23]

In this study, a linear polyimide chain (PTCDA-DCH), chiral MOF (Zn-Dcam-dabco), and Fc quencher were used to develop a novel ECL-based chiral sensor. The system achieved precise ECL signal modulation through electron transfer between PTCDA-DCH and Fc, while leveraging the enantioselective recognition capability of the CMOF to realize highly sensi-

* Corresponding authors, E-mail: chm_kuangx@ujn.edu.cn (X.K.)
E-mail: kuangr1985@foxmail.com (R.K.)

Received June 9, 2025; Accepted August 2, 2025; Published online October 16, 2025

tive and selective detection of histidine enantiomers. Specifically, D-histidine (D-His) exhibits stronger binding energy with the CMOF, preferentially occupying chiral sites and displacing Fc molecules. This competitive adsorption triggered differential ECL signal recovery, enabling efficient enantiomer discrimination. This strategy provides an innovative solution for chiral analyses in pharmaceutical research, food safety monitoring, and biomedical applications.

## EXPERIMENTAL

### General

The materials, reagents and apparatus used in this study are described in detail in the electronic supplementary information (ESI).

### Synthesis of PI

PTCDA-DCH was synthesized using a solvothermal method. 3,4,9,10-perylene tetracarboxylic dianhydride (PTCDA, 0.5 mmol/L) binds to para-cyclohexanediamine (1,4-DCH, 1.5 mmol/L) in the presence of imidazole (25 mmol/L). The mixture was heated at a controlled temperature of 120 ℃ for 24 h to promote condensation. After the reaction, the system was gradually cooled to 85 ℃, at which time the product was washed with deionized water and ethanol to remove the starting raw material and red by-products of the reaction, and a dark red precipitate was collected. The synthesized PI was then dried under high vacuum conditions to ensure complete removal of the solvents (Scheme 1).

### Preparation of Zn-Dcam-dabco MOF

The synthesis of the Zn-Dcam-dabco crystals in this study differs from the previously reported method and incorporates certain improvements.[24] Typically, The mixture of $Zn(NO_3)_2{\cdot}6H_2O$ (150 mg, 0.5 mmol), (+)-$H_2$camph (100 mg, 0.5 mmol) and 0.25 mmol dabco in 5 mL of *N*,*N*-dimethylformamide (DMF) was heated in the screwed-cap teflone vial in a high subkettle at 110 ℃ for 2 days. Block-shaped crystals were collected, washed with DMF and dried in air (Scheme 2).

## RESULTS AND DISCUSSION

### Synthesis and Characterization of the PTCDA-DCH

The structural model of the synthesized one-dimensional PTCDA-DCH material was carefully simulated using the Materials Studio software, and the potential structure was screened and compared. The results indicated that the most likely structure was the AB stack. The structural units are connected in the *X*-direction, and the adjacent 1D chains are stacked *π*–*π* in the *Z*-axis 45° direction (Fig. 1a, Figs. S1–S3 in ESI). Prominent feature peaks of PTCDA-DCH were located (Fig. 1b, Fig. S4 in ESI). In addition, it can be seen that the plane (1,0,0) (2,0,0) (2,0,-1) (5,1,1) corresponding to the reflection peak is well matched with the simulated reflection, and the Pawley refining shows that the difference between the simulated and experimental powder X-ray diffractometry (PXRD) patterns is negligible. The cell parameters obtained by Rietveld were $a$=20.4202 Å, $b$=9.8938 Å, $c$=7.2066 Å, $\alpha$=90°, $\gamma$=90°, $\beta$=85.71° ($R_{wp}$=9.56%, $R_p$=7.49%). Fig. S5 (in ESI) shows the congruence between the PXRD patterns of the synthesized and simulated Zn-Dcam-dabco. $Zn_2$ units were connected in two dimensions *via* rigid chiral camphorate dicarboxylic bridges into infinite planar layers of zinc(II) camphorate [$Zn_2camph_2$] with a square-grid topology.

The morphology of PTCDA-DCH was characterized by scanning electron microscopy (SEM). As shown in Figs. 2(a) and 2(b), PTCDA-DCH was stacked by numerous fibrous nanorods with a length of approximately 600 nm. In the stacking process, many tiny pores are formed, providing more edge ac-

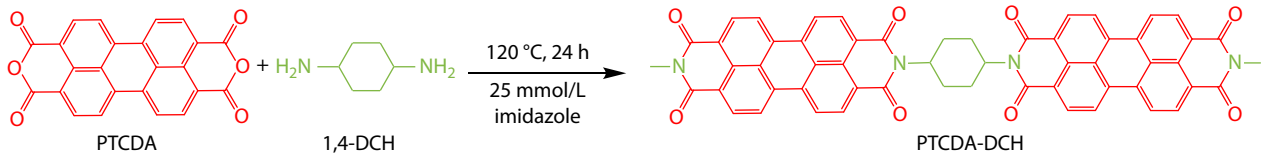


**Scheme 1** Preparation of PTCDA-DCH.

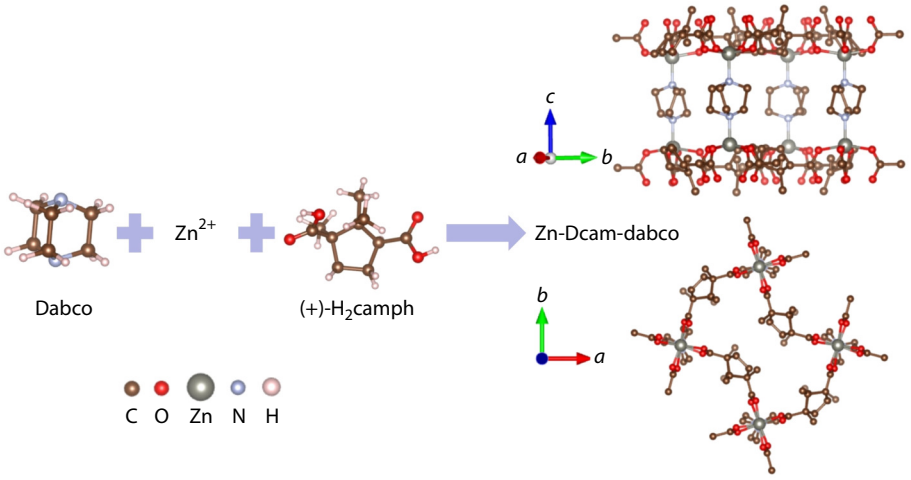


**Scheme 2** Preparation of Zn-Dcam-dabco MOF.

https://doi.org/10.1007/s10118-025-3425-4

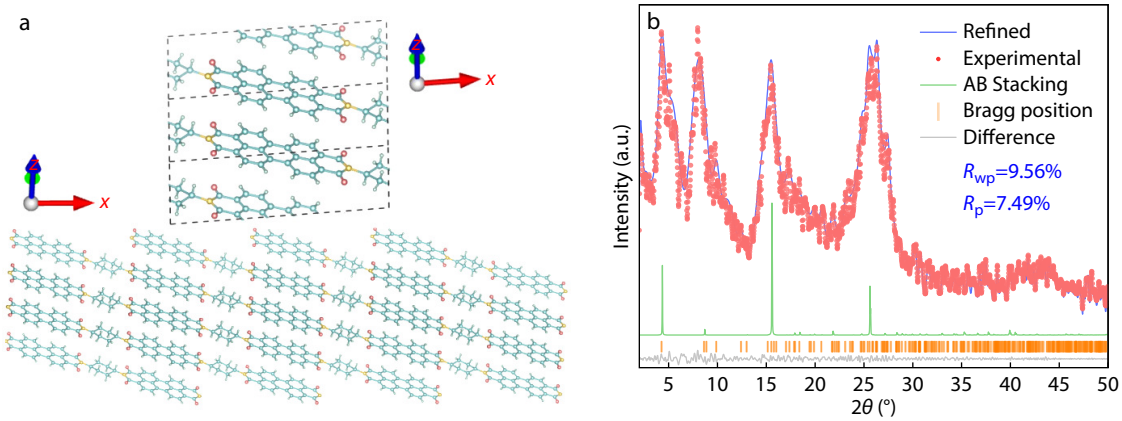


**Fig. 1** (a) Simulated PTCDA-DCH AB cell model and AB stack model; (b) XRD patterns of PTCDA-DCH (red curve) and simulated standard spectrum (green curve).

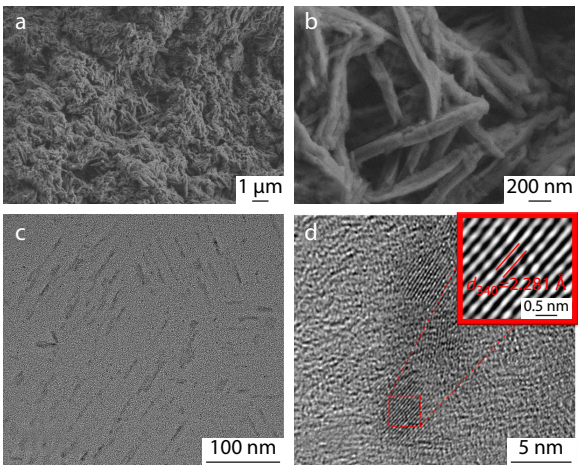


**Fig. 2** (a, b) SEM and (c, d) HR-TEM images at different magnifications of PTCDA-DCH.

tive sites that are conducive to electrochemical sensing. High-resolution transmission electron microscopy (HR-TEM) images revealed that PI had a consistent rod-like structure (Fig. 2c). The lattice fringe spacings of all the synthetic PI can be clearly identified, confirming their highly ordered structure (Fig. 2d). The Zn-Dcam-dabco MOF displayed a hierarchical architecture formed by the stacking of polydisperse nanohexahedrons, creating substantial interstitial spaces (Fig. S6 in ESI). The pore structure of PTCDA-DCH was examined *via* $N_2$ adsorption at 77 K. The PI sample exhibited a Type III isotherm, indicative of a mesoporous material, where gas adsorption primarily occurred through monolayer formation on the surface of the material without a distinct capillary condensation step (Fig. S7 in ESI). The specific surface area was determined to be 132.46 $m^2/g$ with an average pore size of 6.097 nm.

The molecular composition and chemical structure of the synthesized PTCDA-DCH were characterized by Fourier transform infrared (FTIR) spectroscopy, as shown in Fig. S8(A) (in ESI). The C—O—C stretching vibrations of PTCDA (1055–973 $cm^{-1}$) and the bending vibrations of the primary amine (—$NH_2$) in 1,4-DCH (1511–1403 $cm^{-1}$) were significantly attenuated in the FTIR spectrum of PTCDA-DCH, while new peaks corresponding to aromatic tertiary amine C—N stretching vibrations (1341 $cm^{-1}$) emerged. These observations confirmed the successful condensation reaction between the monomers. Fig. S8(B) (in ESI) shows the FTIR spectrum of the Zn-Dcam-dabco MOF. The Zn—O stretching vibration observed at 512 $cm^{-1}$ confirms the coordination between the $Zn^{2+}$ ions and carboxyl groups (—COOH). The broad peak at 3440 $cm^{-1}$ corresponds to residual uncoordinated —OH groups. Characteristic symmetric and asymmetric stretching vibrations of —COOH groups appeared at 1405 and 1626 $cm^{-1}$, respectively. Notably, the splitting of the peak at 1626 $cm^{-1}$ provides clear evidence of the successful coordination state and framework formation in the MOF structure.

The optical properties of PTCDA-DCH dispersed in ultrapure water were investigated by ultraviolet-visible (UV-Vis) spectroscopy (Fig. S9 in ESI). The weak contribution observed at about 300–400 nm originates from the $n\rightarrow\pi$ transition of the anhydride C=O groups. The intense absorption peak at about 400–500 nm was attributed to the highly conjugated macrocyclic $\pi$-system of the perylene core, exhibiting a significant red shift due to electron delocalization.

Furthermore, to gain a deeper insight into the optical interactions between ferrocene (Fc) and PI, the UV-Vis spectrum of Fc was analyzed (Fig. S10 in ESI). The characteristic $\pi\rightarrow\pi^*$ transition of the cyclopentadienyl ligand ($Cp^-$) is observed in the about 300–350 nm range. The absorption in the about 360–530 nm range may be assigned to metal-to-ligand charge transfer (MLCT), reflecting the transfer of d-electrons from Fe(II) to the antibonding $\pi^*$ orbitals of the Cp rings.

## ECL Behaviors of PTCDA-DCH

The electrochemical performance of the modified glassy carbon electrode (GCE) was systematically evaluated using cyclic voltammetry (CV) in a 0.1 mol/L KCl electrolyte solution containing 5 mmol/L potassium ferricyanide/ferrocyanide ($[Fe(CN)_6]^{3-/4-}$) to characterize its redox activity and interfacial electron transfer kinetics. As shown in Fig. S11(A) (in ESI), compared with bare GCE, the REDOX peak intensity of modified GCE at 0.3 V and 0.15 V was significantly reduced, and the REDOX peak value of MOF-Fc GCE was shifted. The MOF/GCE exhibited the weakest REDOX peak current overall, which was slightly enhanced following surface modification with ferrocene (Fc) and PTCDA-DCH. Electrochemical impedance spectroscopy (EIS) measurements

https://doi.org/10.1007/s10118-025-3425-4

revealed the following charge-transfer resistance (Rct) order: MOF/GCE (about 12,951 Ω) > MOF-Fc/GCE (about 5,427 Ω) > MOF-Fc-PTCDA-DCH/GCE (about 4,077 Ω) > bare GCE (about 138 Ω), which was consistent with the CV results (Fig. S11B in ESI). The integration of MOF, Fc and PTCDA-DCH significantly enhanced charge transfer in the sensing system, thereby improving the ECL sensing performance.

Fig. 3 presents a comprehensive analysis of the intensity-potential curve and CV response of ECL for the PTCDA-DCH GCE and bare GCE with and without the co-reactant $K_2S_2O_8$, respectively. Under the presence of a co-reactant, the CV curves of PTCDA-DCH GCE (red curve) and bare GCE (blue curve) began to rise at 0.1 V and reached their peaks at –0.6 V, with the bare GCE exhibiting a lower peak current. The strong ECL potential curve indicates that the PTCDA-DCH GCE (red curve) emits an ECL signal from a threshold voltage of –0.1 V, whereas the bare GCE emits almost no ECL. Fig. S10(B) (in ESI) provides a parallel comparison. The maximum reduction peak of the PTCDA-DCH GCE remains at –0.6 V, while there was no significant reduction peak for the bare GCE. In the absence of $K_2S_2O_8$, neither electrode emitted an ECL signal. The results show that the co-reactant $K_2S_2O_8$ can significantly enhance the ECL emission performance of PTCDA-DCH.

The ECL process initiates at –0.1 V with the reduction of $K_2S_2O_8$ (Eq. 1). As depicted in Eq. 2, when the potential reaches –0.6 V, PTCDA-DCH transformed into its radical anion form PTCDA-DCH$^{\bullet-}$. Subsequently, this radical anion interacts with the sulfate radical anion ($SO_4^{\bullet-}$), generating an additional sulfate ion ($SO_4^{2-}$) and producing the excited state of PTCDA-DCH*, as described in Eq. 3. Finally, the excited PI returns to its ground state through photon emission (hv), which constitutes an observable ECL signal (Eq. 4). The underlying chemical reactions are as follows:

$$S_2O_8^{2-} + e^- \rightarrow SO_4^{2-} + SO_4^{\bullet-} \quad (1)$$

$$\text{PTCDA-DCH} + e^- \rightarrow \text{PTCDA-DCH}^{\bullet-} \quad (2)$$

$$\text{PTCDA-DCH}^{\bullet-} + SO_4^{\bullet-} \rightarrow SO_4^{2-} + \text{PTCDA-DCH}^* \quad (3)$$

$$\text{PTCDA-DCH}^* \rightarrow \text{PTCDA-DCH} + hv \quad (4)$$

## ECL Enantioselective Sensing of His

To explore the regulatory mechanisms of multiple factors on the electrode conductivity, multivariate optimization experiments were conducted. The study revealed that an excessive PI concentration adversely affects electrode conductivity and may induce quenching effects, leading to a reduction in the ECL signal. The optimal PI concentration was determined to be 3 mg/mL, based on ECL intensity analysis shown in Fig. S12(A) (in ESI). Additionally, the optimization of $K_2S_2O_8$ concentration in PBS identified 0.1 mmol/L to yield the maximum ECL signal difference (Fig. S12B in ESI), which was selected for subsequent experiments. Furthermore, to optimize the pH conditions for His enantiomer recognition, investigations across pH 5.6–8.34 revealed critical pH-dependent behaviors (Fig. S12C in ESI). Alkaline conditions (pH>7.5) significantly attenuated ECL intensity due to surface charge variations, whereas acidic environments (pH<7.0) impaired enantioselectivity through protonation-induced changes at chiral binding sites. The pH 7.38 emerged as the optimal compromise, which balances signal stability with stereochemical recognition efficiency, has emerged as the opti-

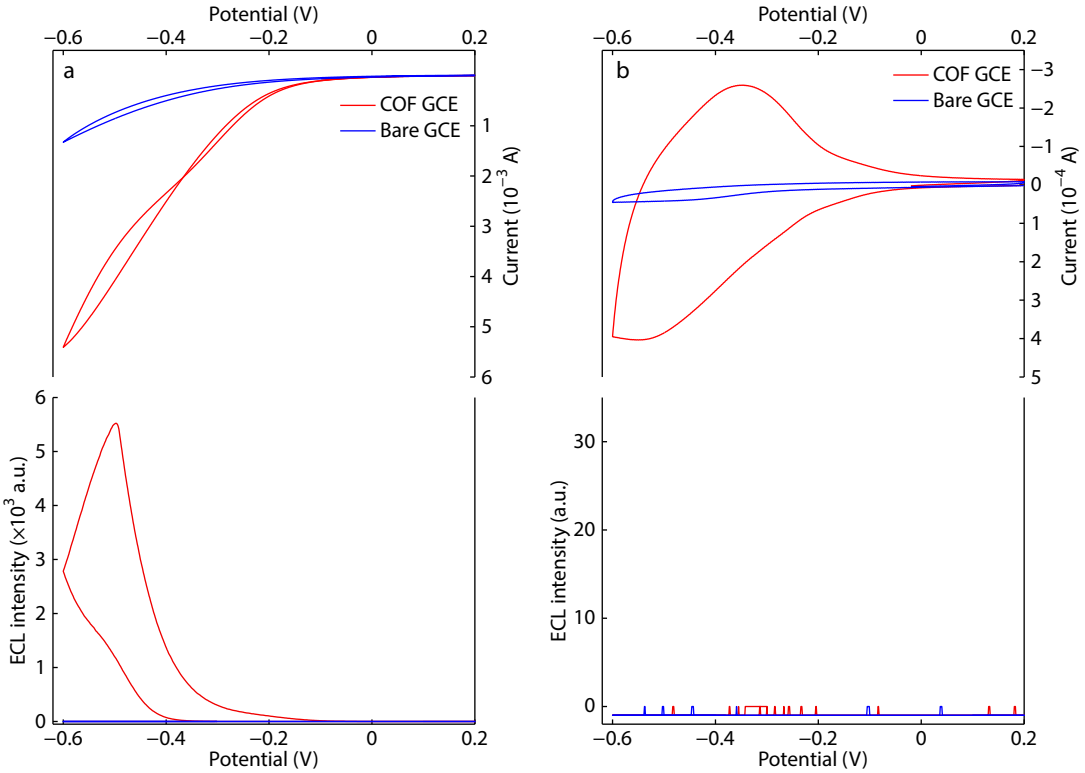


**Fig. 3** CV curves and corresponding ECL-potential curves of bare GCE and PTCDA-DCH/GCE in 0.1 mol/L PBS (a) with and (b) without 0.1 mol/L $K_2S_2O_8$. Scanning rate was set at 0.02 V·s$^{-1}$.

https://doi.org/10.1007/s10118-025-3425-4

mal compromise.

The sensor demonstrated enantioselective ECL sensing through His-triggered Fc displacement from MOF sites (Fig. 4a), with L/D-His exposure amplifying the emission intensity, a phenomenon validated by spectral analysis (Fig. S13 in ESI). Competitive binding studies *via* DPV (Fig. S14 in ESI) revealed critical electrochemical signatures: bare MOF/GCE showed a 0.75 V oxidation peak, while MOF-Fc/GCE displayed characteristic Fc oxidation at 0.06 V.[25] The correlation between Fc concentration and DPV current signal was investigated. The results demonstrated a strong linear relationship between the Fc concentration and the peak current in the DPV (Fig. S15 in ESI). His-MOF interactions caused Fc peak current reduction, with D-His inducing greater Fc desorption than L-His, directly correlating with ECL response differences. This preferential D-His adsorption was evidenced by Fc dissociation dynamics and matched the computational binding affinity predictions (Fig. 5), confirming the stereospecific recognition mechanism.

The analytical performance of the system was further evaluated by quantitatively determining the concentrations of L-His and D-His under optimal conditions. The ECL intensity was found to be proportional to His concentration. Moreover, a strong linear correlation between ECL intensity and D/L-His concentration was observed in the range of 50 μmol/L–2 mmol/L (Figs. 4b and 4c). The linear regression equations for L-His and D-His were $ECL_{D\text{-}His}$ = 4910C (mmol/L) + 1564 ($R^2$ = 0.9998) and $ECL_{L\text{-}His}$ = 1052*C* (mmol/L) + 1570 ($R^2$ =0.9705), respectively. The limits of detection (LOD) for D-His and L-His were calculated to be 0.0029 and 0.0080 mmol/L, respectively, at a signal-to-noise ratio of 3. Compared with previously reported probes and methods for detecting His enantiomers, the probe developed in this study exhibited superior performance in target molecule detection. Notably, it demonstrated a lower detection limit and enhanced signal contrast, indicating improved sensitivity for trace-level analysis. Furthermore, the wide linear range of the probe is particularly suitable for low-concentration measurements, offering distinct advantages for practical applications (Table S2 in ESI).

To further investigate the sensor performance, we systematically evaluated the stability and reproducibility of the ECL sensor for chiral discrimination of His isomers (Fig. 6). The ECL system demonstrated remarkable stability, as evidenced by the highly consistent signals observed during the continuous cyclic voltammetric scans (*n*=10) in the presence of both L-His and D-His. The calculated RSD values of 1.87% for L-His and 1.86% for D-His further confirm the excellent reproducibility of the system. These conclusive results unambiguously validated the efficacy and reliability of the developed ECL sensor for the precise detection of His enantiomers.

## Possible Discrimination Mechanism

Fig. S16 (in ESI) shows UV-Vis absorption spectrum of Fc and ECL spectrum of PTCDA-DCH. Clearly, there was no overlap between the two spectra, indicating that there was no resonance energy transfer between Fc and PTCDA-DCH.[26–28] Fc can dynamically quench PI electrochemiluminescence through electron transfer directly (Eq. 5), accelerating PTCDA-DCH* excited-state decay. This CT process synergizes with $Fc^+$ reduction at -0.6 V (Eq. 6), creating regenerative quenching cycles.[29]

$$Fc + PTCDA\text{-}DCH^* \rightarrow Fc^+ + PTCDA\text{-}DCH^{\bullet -} \quad (5)$$

$$Fc^+ + e^- \rightarrow Fc \quad (6)$$

The distinct wetting behaviors observed in Fig. S17 (in ESI) confirm the selective affinity of the MOF toward His enantiomers. Evidently, the electrode maintained its hydrophobicity by restricting the adsorption of L-His. In contrast, the interaction with D-His is considerably stronger, leading to a reduction in the hydrophobicity of the MOF surface.

Density functional theory (DFT) was employed to investigate the molecular-level adsorption mechanism between the MOF and D/L-His. Distance measurements between the carboxyl group of His and the coordinating oxygen atoms in the MOF, which are 2.16 Å for D-His and 2.081 Å for L-His (Fig. 5). DFT calculations revealed that the binding energies between the MOF and D-His/L-His were −25.74 kcal/mol and −0.19 kcal/mol, respectively, indicating a stronger adsorption affinity of the MOF for D-His.

## Selective Testing and Practical Application

To verify the specificity of the sensor for histidine (His) enantiomers, a series of control experiments was conducted with various enantiomers, including carnitine (Car), methionine (Met), glutamate (Glu), phenylalanine (Phe), proline (Pro), valine (Val),

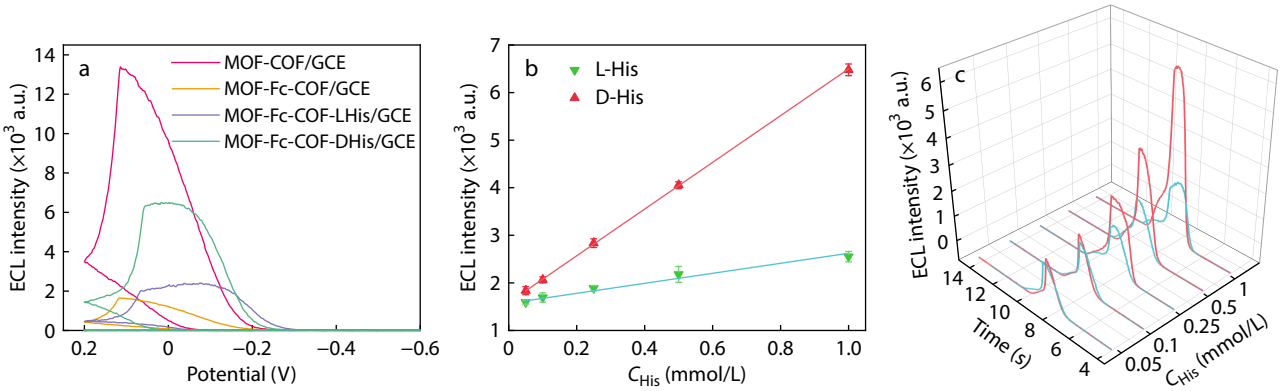


**Fig. 4** (a) ECL intensity–time curve of MOF-Fc-PTCDA-DCH/GCE in the presence of 2 mmol/L L/D- His, MOF- PTCDA-DCH /GCE and MOF-Fc-PTCDA-DCH /GCE with 0.1 mmol/L $K_2S_2O_8$ at pH =7.38 measured by the working electrode. (b) Linear relationship between the ECL signals and the concentrations of L-His and D-His. Error bars =SD (*n* = 3). (c) ECL curves of the constructed sensor toward the identification of D-His and L-His with various concentrations from 50 μmol/L to 2 mmol/L.

https://doi.org/10.1007/s10118-025-3425-4

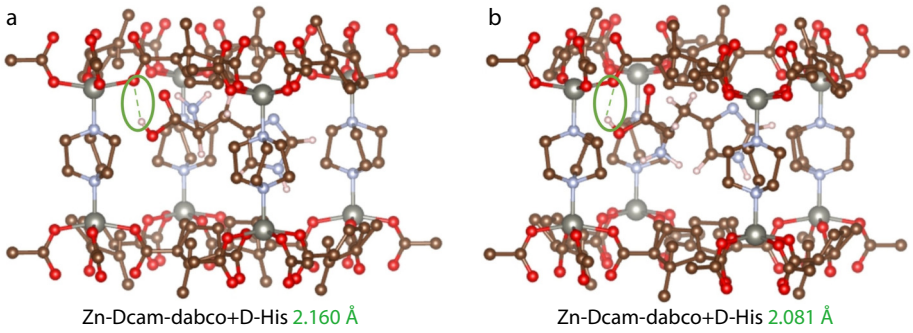


**Fig. 5** Adsorption patterns and binding energy between Zn-Dcam-dabco and (a) D-His and (b) L-His.

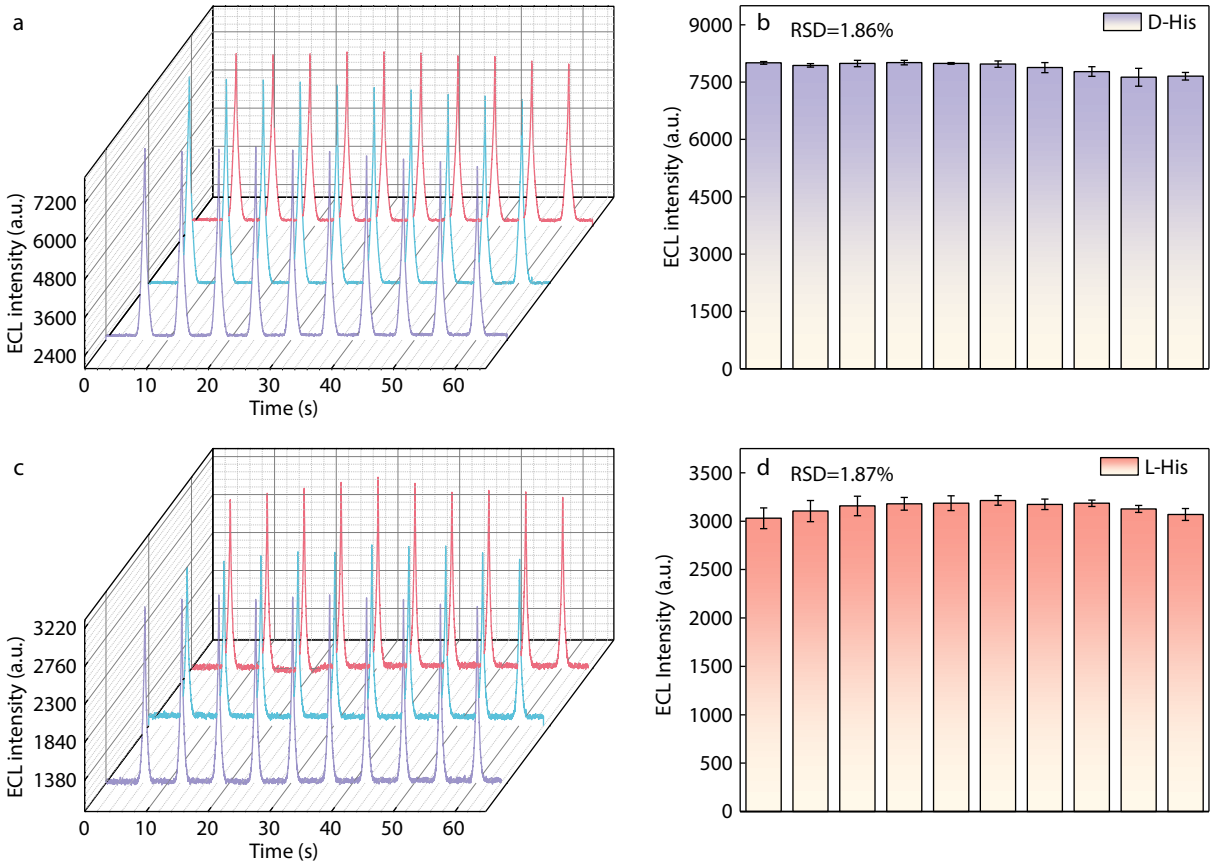


**Fig. 6** The stability and reproducibility of (a, b) D-His and (c, d) L-His were evaluated by the sensor. The error bar represents the standard deviation ($n$=3).

serine (Ser), tyrosine (Tyr), tryptophan (Trp), alanine (Ala), penicillamine (Pen), carnitine (CN), tartaric acid (Tar), and mandelic acid (MN). Each of the amino acid enantiomers was tested at a concentration of 2 mmol/L to ensure a consistent baseline for comparison. As shown in Fig. S18 (in ESI), the disparity in enantiomer signals for other enantiomers, excluding His, was minimal, thereby indicating the proficiency of the proposed method in selectively identifying His enantiomers.

To evaluate the practical efficacy of the established chiral detection sensor, the PTCDA-DCH GCE was used for ECL detection of a racemic mixture of His isomers, maintaining a total concentration of 1 mmol/L. The experimental results showed a linear correlation between the ECL signal and percentage of D-His in the mixture, thereby confirming the precise identification of the enantiomer His racemic mixture (Fig. S19 in ESI). To assess the practicality of the sensor, it was used for the standard addition analysis of His in milk samples, with defined amounts of D-His and L-His added. As summarized in Table S3 (in ESI), the recovery rates ranged from 92.0% to 95.9% for D-His and from 98.0% to 104% for L-His. Compared with existing methods, the proposed approach demonstrates superior applicability for the enantioselective recognition of His enantiomers (Table S4 in ESI), confirming its exceptional practicality and reliability in stereoselective detection.

## CONCLUSIONS

In summary, we developed a novel ECL-based chiral sensor that

https://doi.org/10.1007/s10118-025-3425-4

employs Zn-Dcam-dabco CMOF as the chiral selector, a newly synthesized one-dimensional PI(PTCDA-DCH) as the ECL emitter, and ferrocene (Fc) as the ECL quencher. The electron transfer effect between PTCDA-DCH* and oxidized Fc ($Fc^+$) was utilized as an ECL signal switch. This enabled precise chiral recognition between ECL and CMOF for the joint identification of the His enantiomer. Concentration gradient tests demonstrated an excellent linear response, enabling the quantitative detection of His with a limit of detection (LOD) of 8 μmol/L. When applied to milk sample analysis, satisfactory recovery rates of 98%–104% for L-His and 92%–95.9% for D-His were achieved. This study presents a highly sensitive and innovative strategy for advancing both chiral recognition and food safety detection technologies.

## Conflict of Interests

The authors declare no interest conflict.

## Electronic Supplementary Information

Electronic supplementary information (ESI) is available free of charge in the online version of this article at http://doi.org/10.1007/s10118-025-3425-4.

## ACKNOWLEDGMENTS

This work was financially supported by the Natural Science Foundation of Shandong Province, China (Nos. ZR2020QB065 and ZR2021MB121).

## REFERENCES

1 Chang, W. X.; Liu, M. Y.; Ren, Q.; Shi, Z. S.; Wang, W.; Nie, J.-Y.; Cai, Z. W. Enantioselective behavior and bioactivity of chiral tebuconazole in apples. *Food Control* **2023**, *153*, 109941.
2 Sardella, R.; Lisanti, A.; Marinozzi, M.; Ianni, F.; Natalini, B.; Blanch, G. P.; Castillo, M. L. R. Combined monodimensional chromatographic approaches to monitor the presence of d-amino acids in cheese. *Food Control* **2013**, *34*, 478-487.
3 Zhong, J.-J.; Xia, L.; Xue, L.; Liu, B.; Zhao, L.; Ye, H.; Li, Z. Analytical method for histamine, urocanic acid isomers, and their precursor histidine in fish sauce based on precolumn dansylation and high-performance liquid chromatography. *Food Control* **2023**, *147*, 109566.
4 Messer, L. F.; Bourne, D. G.; Robbins, S. J.; Clay, M.; Bell, S. C.; Mclloroy, S. J.; Tyson, G. W. A genome-centric view of the role of the acropora kenti microbiome in coral health and resilience. *Nat. Commun.* **2024**, *15*, 2902.
5 Morte, L. B.; Moniente, M.; Ramirez, Y. G.; Virto, R.; Gonzalo, D. G.; Pagan, R. Identification by means of molecular tools of the microbiota responsible for the formation of histamine accumulated in commercial cheeses in spain. *Food Control* **2022**, *133*, 108595.
6 Zhang, J. H.; Liang, R. X.; Huang, B.; Yu, L. Q.; Chen, J.; Wang, B. J.; Xie, S. M.; Yuan, L. M. Preparation of a homochiral metal-organic cage and its bonded silicas for efficient enantioseparation in high-performance liquid chromatography and gas chromatography. *Chin. Chem. Lett.* **2025**, 111146.
7 Kobidze, G.; Sprega, G.; Faro, A. F. L.; Balloni, A.; Peluso, P.; Farkas, T.; Karckhadze, M.; Basile, G.; Busardo, F. P.; Chankvetadze, B. Insights into the separation, enantioseparation and recognition mechanisms of methamphetamine isotopologues on achiral and polysaccharide-based chiral columns in high-performance liquid chromatography. *Anal. Chim. Acta* **2025**, *1337*, 343542.
8 Gogolashvili, A.; Tatunashvili, E.; Chankvetadze, L.; Giunashvili, L.; Hefnawy, M.; Ali, I. Chiral separation of pharmaceuticals and agrochemicals using capillary electrophoresis: Migration order, modeling and chiral recognition mechanism. *Talanta* **2025**, *293*, 128004.
9 Zhang, Q.; Ren, S.; Xue, S.; Li, A.; Liu, S.; Sun, X. Tetraalkylammonium-l-tartrate ionic liquids as sole chiral selectors in capillary electrophoresis. *Sep. Purif. Technol.* **2021**, *256*, 117842.
10 Lee, K. W.; Hassan, A. H. E.; Jeong, Y.; Yoon, S.; Kim, S. H.; Lee, C. J.; Jeon, H. R.; Chang, S. W.; Kim, J. Y.; Jang, D. S.; Kim, H. J.; Cheong, J.-H.; Lee, Y.-S. Enantiopure methoxetamine stereoisomers: Chiral resolution, conformational analysis, UV-circular dichroism spectroscopy and electronic circular dichroism. *New J. Chem.* **2021**, *45*, 4354–4364.
11 Gao, L.; Hu, X.; Qin, S.; Chu, H.; Zhao, X.; Wang, B. L-cysteine modified metal–organic framework as a chiral stationary phase for enantioseparation by capillary electrochromatography. *RSC Adv.* **2022**, *12*, 6063–6075.
12 Wang, D.; Wang, P.; Liang, Z.; Li, Z.; Liu, N.; Ma, Q. Novel Cu nanocluster superlattice/mbene-induced ecl enhancement strategy for mirna-221 detection. *Chem. Eng. J.* **2023**, *478*, 147512.
13 Zhai, T.; Zhang, Q.; Yang, F.; Zhou, H.; Hao, T.; Guo, Z.; Chen, Z. A green EC/ECL dual-mode biosensing platform for detection of vibrio parahaemolyticus. *Sens. Actuators B Chem.* **2024**, *415*, 136010.
14 Wang, J.; Han, Z.; Shang, T.; Feng, Y.; Liu, R.; Lu, X. Artemisinin: A novel chiral electrochemiluminescence luminophore-assisted enantiospecific recognition and mechanism identification. *Chem. Sci.* **2024**, *15*, 5581–5588.
15 Wang, Z.; Ren, Y.; Zhou, B.; Chen, Z.; Wang, Z.; Wang, J.; Wang, J. Rapid determination for tyrosine isomers in food based on N-acetyl-l-cysteine/upconversion nanomaterials target-induced quench by chiral electrochemiluminescence sensor. *Food Chem.* **2025**, *463*, 141169.
16 Zhang, W.; Cui, X.; Li, F.; Yan, W.; Wang, Y.; Shang, L.; Ma, R.; Jia, L.; Li, C.; Wang, H. Perylene diimide and g-$C_3N_4$ nanosheet as potential-resolved cathode luminophores for ultrasensitive ratiometric electrochemiluminescence immunosensor. *Sensor Actuat B-Chem* **2022**, *371*, 132492.
17 Zhao, L. Y.; Zhao, H. Q.; Shang, L.; Shen, G. D.; Ma, R. N.; Wang, H. S. A robust ECL-enhanced system based on UiO-66-COOH promoting perylene diimide derivative electrochemiluminescence for tumor biomarker detection. *Sensor Actuat B-Chem* **2025**, *423*, 136824.
18 Zhang, Y.; Li, Z.; Du, J.; Jie, G.; Zhou, H. Potential-resolved ratio electrochemiluminescence biosensor based on perylene diimide-MOF and DNA nanoflowers–CdS quantum dots for detection of dual targets. *Anal. Chem*, **2024**, *96*, 13690–13698.
19 Cao, W.; Ferrance, J. P.; Demas, J.; Landers, J. P. Quenching of the electrochemiluminescence of tris(2,2′-bipyridine)ruthenium(II) by ferrocene and its potential application to quantitative DNA detection. *J. Am. Chem. Soc.* **2006**, *128*, 7572–7578.
20 Sha, H.; Zhang, Y.; Wang, Y.; Ke, H.; Xiong, X.; Xue, H.; Jia, N. Electroluminescent aptasensor based on $RuSiO_2$ nanoparticles for detection cytochrome c using ferrocene as quenching probe. *Biosens. Bioelectron.* **2019**, *132*, 203–209.
21 Thoonen, S.; Siripanich, P.; Hua, L.; Tay, H. M.; Ramkissoon, P.; Smith, T. A.; Lessio, M.; Hua, C. Enhancing enantioselectivity in

chiral metal organic framework fluorescent sensors. *Inorg. Chem. Front.* **2024**, *11*, 3877–3888.
22 Ye, N.; Ma, J.; An, J.; Li, J.; Cai, Z.; Zong, H. Separation of amino acid enantiomers by a capillary modified with a metal–organic framework. *RSC Adv.* **2016**, *6*, 41587–41593.
23 Zhao, X.; Nguyen, E. T.; Hong, A. N.; Feng, P.; Bu, X. Chiral isocamphoric acid: Founding a large family of homochiral porous materials. *Angew. Chem. Int. Ed.* **2018**, *57*, 7101–7105.
24 Dybtsev, D. N.; Yutkin, M. P.; Peresypkina, E. V.; Virovets, A. V.; Serre, C.; Ferey, G.; Fedin, V. P. Isoreticular homochiral porous metal–organic structures with tunable pore sizes. *Inorg. Chem.* **2007**, *46*, 17.
25 Hatamluyi, B.; Sadeghzadeh, S.; Sadeghian, R.; Mirimoghaddam, M. M.; Boroushaki, M. T. A signal on-off ratiometric electrochemical sensing platform coupled with a molecularly imprinted polymer and $CuCo_2O_4$/NCNTs signal amplification for selective determination of gemcitabine. *Sens. Actuators B Chem.* **2022**, *371*, 132552.
26 Chu, Y.; Han, T.; Deng, A.; Li, L.; Zhu, J. J. Resonance energy transfer in electrochemiluminescent and photoelectrochemical bioanalysis. *TrAC Trends Anal. Chem.* **2020**, *123*, 115745.
27 Wang, X.; Jia, C.; Wang, S.; Dong, Y. Coreactant-free strong $Ru(bpy)_3^{2+}$ ECL at ionic liquid modified electrode and its application in sensitive detection of glucose based on resonance energy transfer. *Talanta* **2024**, *270*, 125584.
28 Yan, Y.; Wang, X. Y.; Hai, X.; Song, W.; Ding, C.; Cao, J.; Bi, S. Chemiluminescence resonance energy transfer: From mechanisms to analytical applications. *TrAC Trends Anal. Chem.* **2020**, *123*, 115755.
29 Yang, X.; Wei, Y.; Wang, Z.; Wang, J.; Qi, H.; Gao, Q.; Zhang, C. ECL highly efficient electrogenerated chemiluminescence quenching on lipid-coated multifunctional magnetic nanoparticles for the determination of proteases. *Anal. Chem.* **2022**, *94*, 2305–2312.

https://doi.org/10.1007/s10118-025-3425-4